













Global ocean wave fields show consistent regional trends between 1980 and 2014 in a multi-product ensemble

L. Erikson ^{1✉}, J. Morim^{1,2,3}, M. Hemer³, I. Young ⁴, X. L. Wang⁵, L. Mentaschi⁶, N. Mori ⁷, A. Semedo ⁸, J. Stopa ⁹, V. Grigorjeva ¹⁰, S. Gulev¹⁰, O. Aarnes¹¹, J.-R. Bidlot¹², Ø. Breivik^{11,13}, L. Bricheno¹⁴, T. Shimura⁷, M. Menendez¹⁵, M. Markina¹⁰, V. Sharmar ¹⁰, C. Trenham ³, J. Wolf ¹⁴, C. Appendini ¹⁶, S. Caires ¹⁷, N. Groll¹⁸ & A. Webb ¹⁹

Historical trends in the direction and magnitude of ocean surface wave height, period, or direction are debated due to diverse data, time-periods, or methodologies. Using a consistent community-driven ensemble of global wave products, we quantify and establish regions with robust trends in global multivariate wave fields between 1980 and 2014. We find that about 30–40% of the global ocean experienced robust seasonal trends in mean and extreme wave height, period, and direction. Most of the Southern Hemisphere exhibited strong upward-trending wave heights (1–2 cm per year) and periods during winter and summer. Ocean basins with robust positive trends are far larger than those with negative trends. Historical trends calculated over shorter periods generally agree with satellite records but vary from product to product, with some showing a consistently negative bias. Variability in trends across products and time-periods highlights the importance of considering multiple sources when seeking robust change analyses.

¹US Geological Survey (USGS), Pacific Coastal and Marine Science Center, Santa Cruz, CA, USA. ²University of Central Florida, Orlando, FL, USA. ³Commonwealth Scientific and Industrial Research Organisation (CSIRO) Oceans and Atmosphere, Hobart, TAS, Australia. ⁴Department of Infrastructure Engineering, University of Melbourne, Melbourne, Australia. ⁵Climate Research Division, Environment and Climate Change Canada, Toronto, ON, Canada. ⁶Department of Physics and Astronomy Augusto Righi, University of Bologna, Bologna, Italy. ⁷Disaster Prevention Research Institute, Kyoto University, Kyoto, Japan. ⁸IHE-Delft, Department of Water Science and Engineering, Delft, The Netherlands. ⁹Department of Ocean and Resources Engineering, University of Hawai'i, Honolulu, HI, USA. ¹⁰P.P. Shirshov Institute of Oceanology of the Russian Academy of Sciences, Moscow, Russia. ¹¹Department of Research and Development, Norwegian Meteorological Institute, Oslo, Norway. ¹²European Centre for Medium-Range Weather Forecasts, Reading, UK. ¹³University of Bergen, Bergen, Norway. ¹⁴National Oceanography Centre, Liverpool, UK. ¹⁵Institute of Hydraulics Cantabria, Santander, Spain. ¹⁶National Autonomous University of Mexico, Mexico City, Mexico. ¹⁷Deltares, Delft, The Netherlands. ¹⁸Helmholtz-Zentrum Hereon, Geesthacht, Germany. ¹⁹Tokyo Institute of Technology, Tokyo, Japan. ✉email: lerikson@usgs.gov

Understanding long-term historical changes in the temporal and spatial structure of wind-generated surface ocean waves are essential to the ocean and coastal applications as well as to quantifying climate variability and change in ocean wind waves and anthropogenic influences on global wave fields^{1,2}. Generated by a combination of basin-wide and local atmospherically forced surface wind patterns, variability, and change in ocean wave fields directly impacts marine structures, coastal populations, economies, and ecosystems^{3,4}. In general, wave climate fields are represented in terms of significant wave height (H_s), mean wave period (T_m), and mean wave direction (θ_m), which are often dominant of coastal flooding and morphologic changes, disrupting ecosystem-level processes⁴ and offshore-coastal industry operations⁵. For example, H_s and T_m are strongly linked to elevated coastal water levels via wave run-up^{6,7}, whilst changes in wave direction control shoreline stability over multiple time scales^{8,9}. Hence, a comprehensive understanding of global multivariate wave climate patterns, and their past changes, is critical to successful planning in anticipation of future needs, particularly given the persistent trend of human migration to coastal regions⁸, the very rapid growth of offshore renewable energy⁹ and fish farming¹⁰, and the dependence on and foreseen increase in the transport of goods across the global ocean¹¹.

Understanding changes in the wave climate is challenging as waves integrate wind properties over space and time and, hence, do not necessarily mirror wind variability¹². Variability and trends in ocean wave height over the last few decades have been explored at global and regional scales using ship observations, buoy measurements, satellite altimetry records, as well as statistical models and dynamic downscaling (numerical wave simulations)^{13–16}. Whereas ship and buoy records are useful sources of regional and/or local data, they are temporally and geographically inhomogeneous and spatially limited and therefore insufficient to offer a globally consistent quantification of historical variability and trends on their own. Satellite wave records are currently the most spatiotemporally comprehensive sources of wave height measurements and have been used to quantify variability and trends in H_s over the last two decades, both globally and regionally^{14,17,18}. Nevertheless, satellite altimetry-retrieved wave data are limited in time from 1985 onwards and tend to underestimate upper-percentile H_s due to temporal sampling inhomogeneity^{18,19}. The accuracy and consistency of multi-mission global satellite wave products likewise depend on calibration methods and the type/quality of algorithms/methods used to address instrument biases, drifts, and discrepancies, resulting in inconsistent wave height trends across satellite-based global products^{18,19}.

In the recent past, multi-decadal simulations of surface wave fields driven by atmospheric surface wind fields, developed to support a variety of climatological assessments, have been used to assess trends in H_s ^{17,20–23}. These simulations yield homogeneous spatial and temporal multivariate data at high resolution, a requirement for comprehensive analysis of wave fields, especially extreme wave events²⁴. Nowadays, there are numerous global wave hindcasts and reanalysis products originating from a range of global atmospheric reanalysis forcing¹⁹. However, existing atmospheric reanalysis products have well-documented biases and inconsistent long-term trends in surface wind fields^{25,26} due to differences in data assimilation schemes and model input data as well as spatial and temporal model resolution and physical parameterizations. As a result, global wave hindcasts and reanalyses produced using different atmospheric reanalyses, often produce disparate and contrasting results²⁷. Furthermore, factors introduced by the complex numerical wave modelling process (such as wind-wave parameterizations, sea-ice forcing fields and/or model resolution) and calibration

procedures further contribute to differences between existing products^{2,28,29}.

Despite such differences, global analyses of long-term historical H_s changes have relied on one or two global wave products to infer variability and trends, thereby limiting resulting conclusions. In addition, most analyses only assess historical changes in H_s , despite the recognized importance of understanding changes in T_m , θ_m , and frequency of storm wave events^{30,31}. Here we use a multi-product ensemble of global wave hindcast/reanalysis products, processed through a community-developed framework^{32,33}, to quantify historical seasonal trends in multivariate global wave fields. In addition to establishing previously unrecognized patterns of historical changes in T_m , θ_m , and frequency of storm wave events, we assess the intrinsic variability between products, providing key insights for broad-scale assessments.

The ensemble used here is made possible by contributions to the Coordinated Ocean Wave Climate Project (COWCLIP)^{32–34} from 10 international research groups. In all, contributed datasets include 12 dynamically downscaled global wave hindcast and reanalysis products, from which 7 members, covering a common 35-year time-period (1980–2014), are used to quantify robust historical trends. In addition, 3 observation-based datasets (2 satellite altimeter wave databases and a voluntary ship observations wave dataset—VOS) are used as references in the inter-comparison analysis. All model members were generated independently and processed through a community-based framework^{32,33} to ensure a consistent analysis (see the “Methods” section). A brief description of each ensemble product is provided in the Methods and their key details are summarized within historical Table 1.

In this analysis, we focus on seasonal trends due to the strong link between seasonal wave regimes and associated offshore and coastal wave-driven risks. The winter/summer seasons of the Northern and Southern Hemispheres are considered here: December–February (DJF) and June–August (JJA), respectively. For each respective season, we consider all combinations of 50th and 90th percentile H_s , T_m , and θ_m . Furthermore, we consider two threshold-based extreme wave indices, proposed by the World Climate Research Programme (WCRP) Expert Team on Climate Change and Detection, which are defined as an annual number of days when daily-max H_s exceeds 2.5 m (rough wave days; hereafter τ_{RO}) and 6.0 m (high wave days; hereafter τ_{HI}).

Results

All global wave model products were re-gridded to a common 0.5° resolution grid for inter-model comparison analysis and to a common 2° grid for direct comparison to altimeter data. Linear trends were computed at each grid cell for each product across the entire globe using Sen’s slope and the Mann–Kendall test for significance (see in the section “Methods” subsection “Model skill statistics”). To decrease the scatter introduced by natural atmospheric cycles on the overall trend, a 3-year running average was applied to each time-series at each grid cell. The ensemble is populated with products that meet the requirement of being longer than 30 years. This requirement plus other findings of temporal step changes in atmospheric forcing (and input conditions) resulted in the selection of 7 members for the ensemble mean (rows 1–7 within Table 1) spanning the years 1980 through 2014 (see in the “Methods” subsections “Ensemble selection” and “Robustness criteria”). Detailed maps of all 12 global wave hindcast and reanalysis products as well as multi-product ensemble means using all 12 members, are given in Supplementary Notes 2 and 3. For the 7-member ensemble, resulting DJF and JJA seasonal trends calculated over 1980–2014 (35-year period) typically lie within ± 2 cm/yr, ± 0.02 s/yr,

Table 1 Summary of wind-wave products considered in this analysis.

ID	Centre-dataset	Atmospheric reanalysis (levels)	Assimilation system and method	Spatial and temporal resolution	Sea-ice model	Spectral wave model	Source-terms (ψ_{max})	Spatial and temporal resolution	Spectral frequency	H_s, T_m, θ_m
1	ECMWF-ERA5 ^b	ERA5 (L137)	IFS 41R2- 4DVAR ^c	0.25°/1h	OSI-SAF (daily)	EC-WAM (Cy41r2)	ST3 (default)	0.36°/1h	360f × 24d	Reanalyses ^b (coupled system)
2	ECMWF-ERA ^b	ERA-Interim (L91)	IFS 31R2- 4DVAR ^c	0.75°/6h	OSI-SAF (daily)	EC-WAM (Cy31r2)	ST3 (default)	1.00°/6h	30f × 24d	H_s, T_m, θ_m
3	ECMWF-ERA5H	ERA5 (L137)	IFS 41R2- 4DVAR	0.25°/1h	ERA5 (daily)	EC-WAM (Cy46r1)	ST4 (default)	0.50°/1h	36f × 36d	H_s, T_m, θ_m
4	KU-JRA55 (1980-2012)	JRA55 (L60)	GSM-4DVAR	0.56°/6h	COBE (monthly)	WW3 (v4.18)	ST4 (default)	0.56°/1h	29f × 30d	Hindcasts (atmosphere reanalysis-forced simulations)
5	IORAS-MERRA2	MERRA2 (L72)	GEOS-5-3DVAR	0.50° × 0.62°/6h	MERRA2 (hourly)	WW3 (v5.16)	ST4 (default)	0.50° × 0.62°/6h	32f × 24d	H_s, T_m, θ_m
6	NOC-ERA1	ERA-Interim (L91)	IFS 31R2- 4DVAR	1.12°/3h	LIM2 of global(daily)	WW3 (v3.14)	ST2 (default)	0.7° × 0.47°/1h	30f × 36d	H_s, θ_m
7	IHC-GOW1.0	NCEP-NCAR (L28)	GDAS/3D-VAR	1.90° × 1.87°/6h	MOM3 (hourly)	WW3 (v2.22)	ST2 (default)	1.50° × 1.0°/6h	25f × 72d	H_s, T_m, θ_m
8	IHC-GOW2.0	CFRS/ (L64)	GDAS/CFSS-3DVAR	0.30°/1h	MOM4 (hourly)	WW3 (v4.18)	ST4 ($\beta = 1.26$)	0.25-0.50°/1h	32f × 24d	H_s, T_m, θ_m
9	CSIRO-CAWCR	CFRS/ (L64)	GDAS/CFSS-3DVAR	0.30°/1h	MOM4 (hourly)	WW3 (v3.14)	ST4 ($\beta = 1.33$)	0.40°/1h	29f × 24d	H_s, T_m, θ_m
10	IFREMER-CFSR ^d	CFRS/ (L64)	GDAS/CFSS-3DVAR	0.30°/1h	MOM4 (hourly)	WW3 (v5.16)	ST4 ($\beta = 1.30$)	0.50°/1h	32f × 24d	H_s, T_m
11	JRC-CFSR	CFRS/ (L64)	GDAS/CFSS-3DVAR	0.30°/1h	None	WW3 (v4.18)	ST4 ($\beta = 1.52$)	1.5°-0.50°/3h	25f × 24d	H_s, T_m, θ_m
12	JRC-ERA1	ERA-Interim (L91)	IFS 31R2- 4DVAR ^c	0.75°/12h	None	WW3 (v4.18)	ST4 (default)	1.0°/12h	25f × 24d	H_s, T_m, θ_m
13	IORAS-VOS						Variable; gridded to 2° × 2°			H_s
14	IMOS (GLOBWAVE/RADS/AVISO/NSOAS and NOAA) ^a (1985-2014)						Variable; gridded to 2° × 2°			H_s
15	ECCI (1995-2014)						Variable; gridded to 2° × 2°			H_s

The description of each product is provided in Supplementary Notes 1. Time-periods cover 1980-2014 unless stated otherwise. Corrupted data of the following statistical summaries were excluded from the analyses: IHC-GOW2.0 DJF and JJA median H_s ; CSIRO-CAWCR θ_m first time-point.
^a T_m is the first moment mean wave period in all products except IFREMER-CFSR for which the second moment mean wave period T_{m02} was provided.
^bCoupled System. Assimilated data within each atmospheric reanalysis product are provided within Supplementary Fig. S1.
^cIFS consolidation cycle.
^dIncludes altimetry wind corrections.

$\pm 0.5^\circ/\text{yr}$, and $\pm 1\text{day}/\text{yr}$ for H_s , T_m , θ_m , τ_{RO} , and τ_{HI} , respectively (Figs. 1–3).

Qualitative assessment of coherent trends between individual products. Inspection of Figs. 1, 2 shows strikingly coherent patterns of increasing H_s trends across the Pacific and Atlantic Oceans for DJF and across all ensemble products. The historical patterns of change for H_s^{50} and H_s^{90} , and both DJF and JJA seasons, are similar except that H_s^{90} generally shows stronger trends. The variability between ensemble products is greater for H_s^{90} during DJF and JJA compared to H_s^{50} as shown by the standard deviation (σ) determined across the multi-product ensemble (bottom rows in Figs. 1, 2). T_m trends upwards across most of the global ocean during both seasons, except in the tropical Eastern Pacific Ocean during DJF (Fig. 1). With regard to θ_m , there is consistency between ensemble members, with clear counter-clockwise (CCW) rotations across the Indian and Equatorial Pacific Oceans, and clockwise (CW) rotation across the Southern Atlantic and Northwestern Pacific Oceans during JJA. For DJF, strong CW θ rotations across the tropical Pacific Ocean are found, contrasted with CCW rotations across the North Atlantic and southern Indian Oceans.

Trend values in an annual number of rough wave days (τ_{RO}) are large ($> \pm 1\text{ day}/\text{yr}$), with widespread increases across the Southern Hemisphere and North Atlantic basin (left column of Fig. 3). There is a downward trending τ_{RO} across the North-Central Pacific Ocean across all products, which is particularly accentuated for KU-JRA55. Whereas all ensemble products exhibit strong upward trends off the west coast of South America, their magnitude contrasts, as shown by σ calculated across the ensemble (bottom row in Fig. 3). In contrast to τ_{RO} , trends in the number of high wave days (τ_{HI}) are limited to extra-tropical areas due to their high-energy forcing regimes. Increasing τ_{HI} trends are shown across all ensemble products off Antarctica except for KU-JRA55 (right column of Fig. 3). In the Northern Hemisphere, all ECMWF products show increasing τ_{HI} trends in the high-latitudes of the North Pacific (Southern Alaska and Siberian Peninsula) and a contrasting decrease to the south which is consistent across all products. Consistent across all ensemble products is also a decrease in τ_{HI} off Greenland.

Quantified robust trends. A quantitative comparison of all 7 ensemble products using a well-established robustness criterion (see the “Methods” section)^{35,36} demonstrates that robust historical trends existed across 15–40% of the global ocean for all variables (H_s , T_m and θ_m) during both seasons between 1980 and 2014 (Figs. 4, 5 and Tables 2–5). Robust trends of τ_{RO} were found across 32% of the global ocean region, whereas τ_{HI} exhibited robust changes only across 10% (Fig. 6 and Table 6). The percentage of the global oceans with robust positive trends is shown to be much greater than those with negative trends, except for θ_m (Tables 4 and 5). For instance, 30–40% of the global ocean region exhibited upward trends in H_s^{50} and H_s^{90} , whereas $< 10\%$ exhibited robust negative trends (Tables 2 and 3). This relationship holds true across most ocean regions except the North Pacific Ocean, where decreasing trends in JJA season H_s^{50} and H_s^{90} dominate (Table 3). Mean incident wave directions (θ_m) rotated CW and CCW across approximately equal areas of the global ocean during both seasons (Tables 4 and 5).

Historical changes to DJF H_s^{50} and H_s^{90} show an overall pattern of positive trends across the Tropics ($0.37\text{--}0.43$ and $0.56\text{--}0.58\text{ cm}/\text{year}$), Southern Ocean ($0.67\text{--}0.75$ and $1.06\text{--}1.16\text{ cm}/\text{year}$) (Table 2), and along the western coastal regions of the North Pacific and North Atlantic Oceans, respectively (Fig. 4). Some regions of

downward H_s trends are found for the North Pacific and North Atlantic basins. The H_s^{50} and H_s^{90} DJF patterns are similar (Fig. 4), but with greater rates of change for H_s^{90} (global average of $0.89 \pm 0.50\text{ cm}/\text{yr}$ compared to $0.58 \pm 0.30\text{ cm}/\text{yr}$) (Table 2). The spatial patterns of H_s^{50} and H_s^{90} JJA are also similar to each other but with stronger signals for extreme H_s^{90} conditions ($0.75 \pm 0.40\text{ cm}/\text{yr}$ compared to $0.53 \pm 0.27\text{ cm}/\text{yr}$, Table 3). Whilst upward H_s trends are ubiquitous across the Southern Hemisphere, exceeding $> 1.5\text{ cm}/\text{yr}$ within particular regions, no robust trend changes are seen within the Indian Ocean for JJA (Fig. 4). All of South America’s coastal areas experienced upward trending H_s JJA (Fig. 4). Robust upward H_s trends are seen off Africa, during both seasons, and along Japan during DJF. In contrast, Europe experienced downward H_s trends during DJF and upward trends, or no change, during JJA. The United States’ western coastline experienced a general decrease, or no change, during DJF and JJA (Fig. 4).

Critical to coastal applications are also T_m and θ_m (Fig. 5). Robust positive T_m trends are found to have occurred primarily over the Southern Ocean, North Atlantic Ocean, and western North Pacific Ocean during DJF and over the South Pacific Ocean and the entire Atlantic Ocean during JJA (Fig. 5a, c). Almost the entire eastern Tropical Pacific Ocean experienced decreased T_m during DJF. In contrast, no robust trends are seen across the Indian, Tropical, and North Pacific basins during JJA (Fig. 5c). In terms of θ_m changes, there is a strong CW rotation across most of the North and Tropical Pacific regions and Tropical Atlantic Ocean during DJF (Fig. 5b, d), sometimes exceeding $0.5^\circ/\text{year}$. In contrast, most of the Southern Hemisphere experienced CCW rotations up to $0.20^\circ/\text{year}$ (Tables 4 and 5), with the strongest CCW rotations found off western South America. Patterns of directional change are scattered for the JJA season, with CCW θ_m rotations across the Indian and Tropical Pacific Oceans and CW rotations within the North Pacific, North Atlantic, and South Atlantic basins (Fig. 5d).

The trend signal in τ_{RO} is large across almost the entire Southern Hemisphere (Fig. 6). The tropical basins experienced growing occurrences of τ_{RO} across 45–50% with a rate of change of 0.62 ± 0.21 to $0.85 \pm 0.42\text{ days}/\text{yr}$ (Fig. 6a; Table 6). The North Atlantic also experienced growing occurrences of τ_{RO} between 0.39 ± 0.12 across 31% of the region (Table 6). In contrast, the central North Pacific basin exhibits a general decrease in τ_{RO} values. Changes in τ_{HI} are limited to the high latitude areas (Fig. 6b) where H_s exceeds 8 m. There is an increased τ_{HI} ranging from 0.36 ± 0.13 to $0.38 \pm 0.29\text{ days}/\text{yr}$, across the Southern Ocean (Table 6) and a decreased τ_{HI} across the central North Pacific region.

Altimeter comparisons and the influence of duration on trends. The ensemble trend computed for this analysis encompasses 35 years from 1980 to 2014, and reflects the longest period of temporally overlapping data across the multi-product ensemble³⁷. At the time of this analysis, the start dates of the two altimeter reference datasets IMOS and ECCI were 1985 and 1995, respectively; to compare individual and ensemble model trends to the satellite altimeter data, all data were re-gridded to a common 2° grid (native resolution of the altimeter reference datasets) and trends computed over three time-periods (Fig. 7): 1980–2014 (35 years), 1985–2014 (30 years), and 1995–2014 (20 years).

Global population means and distributions of trends across the three time-periods and for each product (Table 1) are summarized in Fig. 7. Figure 7 demonstrates that historical trends are highly sensitive to the duration of the record, being likely influenced by the modes of the decadal and inter-decadal ocean and atmospheric

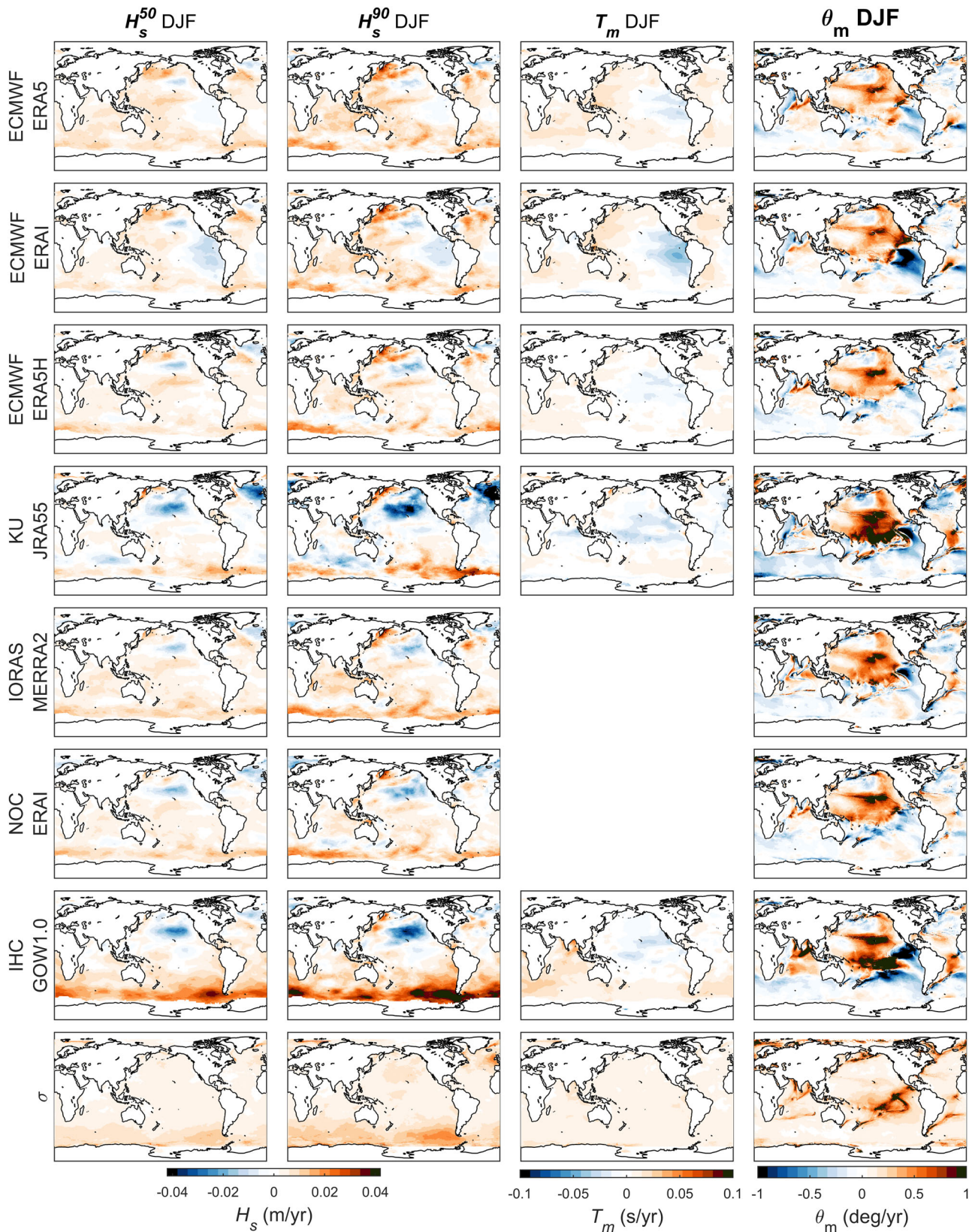


Fig. 1 Boreal winter trends. Boreal winter (December through January, DJF) trends of median and 90th percentile significant wave heights (H_s^{50} and H_s^{90}), median of mean periods (T_m), and median of mean directions (θ_m) for each individual reanalysis and hindcast products used in the 7-member ensemble for 1980–2014. T_m data were not available for NOC and IORAS (Table 1).

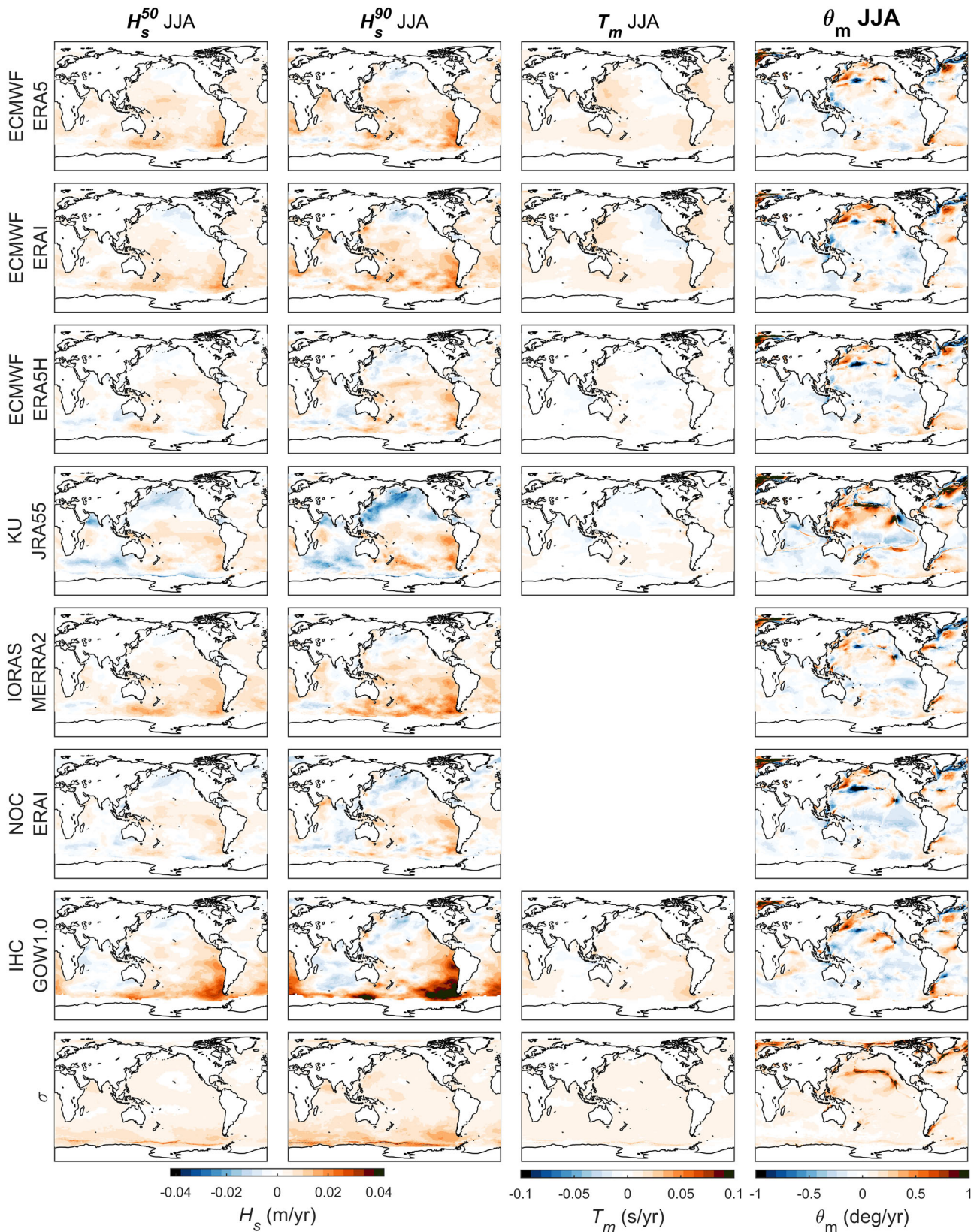


Fig. 2 Austral winter trends. Austral winter (December through January, JJA) trends of median and 90th percentile significant wave heights (H_s^{50} and H_s^{90}), a median of mean periods (T_m), and median of mean directions (θ_m) for each individual reanalysis and hindcast products used in the 7-member ensemble for 1980–2014. T_m data were not available for NOC and IORAS (Table 1).

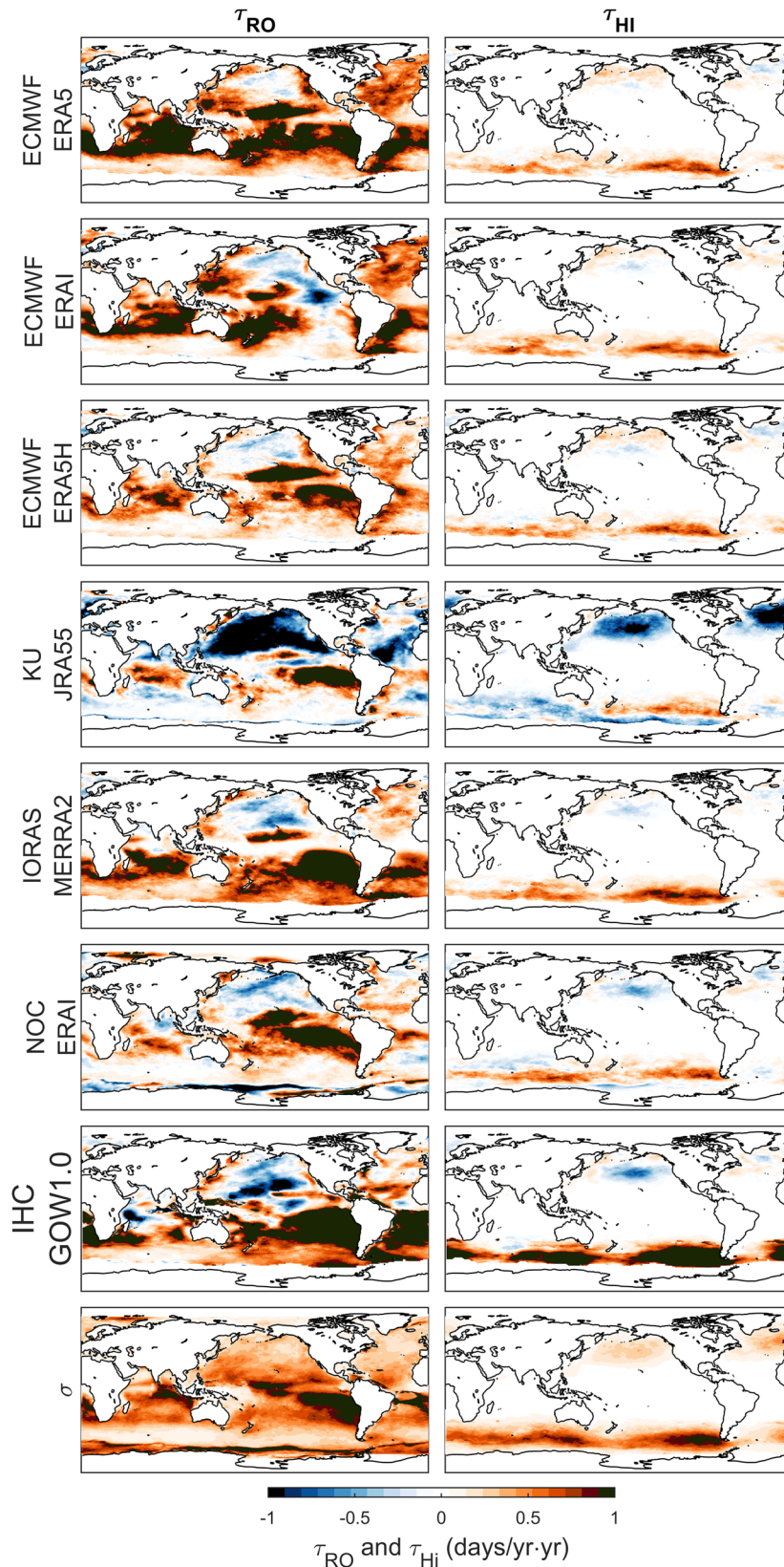


Fig. 3 Trends in the frequency of high wave events. Trends in an annual number of rough (τ_{RO}) and high wave days (τ_{HI}) for each individual reanalysis and hindcast products used within the 7-member ensemble for 1980–2014.

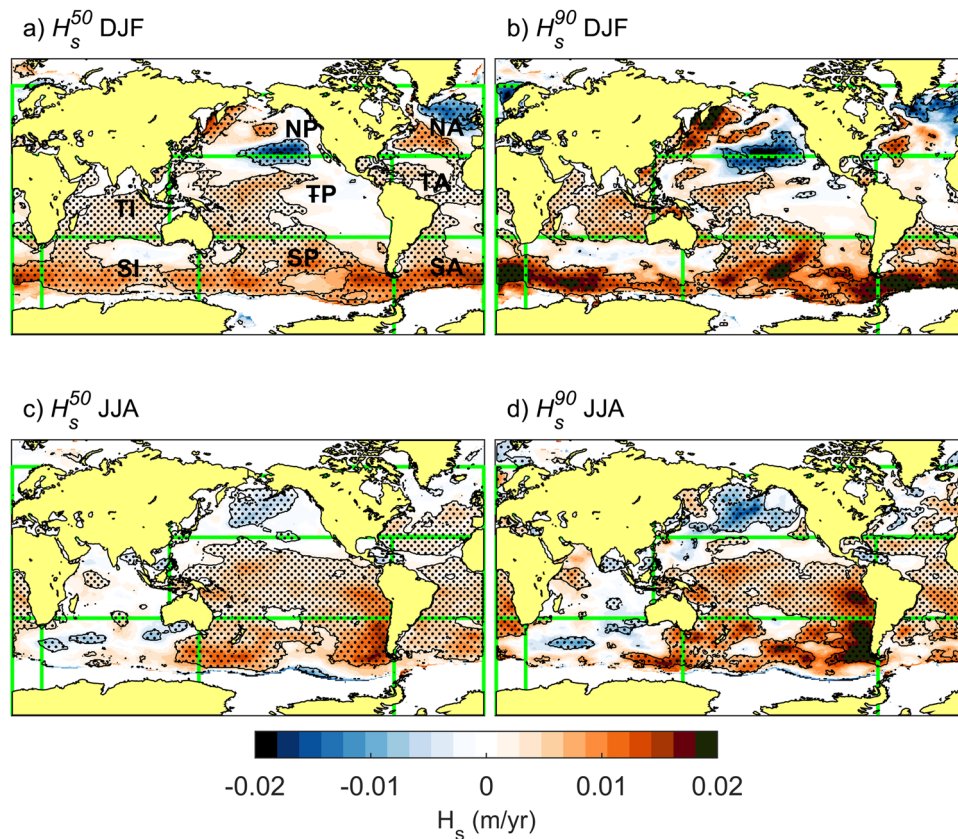


Fig. 4 Significant wave height (H_s) trends based on the 7-member ensemble for 1980–2014. a Median DJF season, **b** 90th percentile DJF, **c** median JJA season, and **d** 90th percentile JJA. Stippling indicates regions of robust trends (multi-member ensemble mean > inter-member standard deviation; see Methods). Green lines delineate large-scale ocean basins (NP: North Pacific; NA: North Atlantic; SP: South Pacific; SA: South Atlantic; SI: South Indian; TP: Tropical Pacific; TA: Tropical Atlantic; TI: Tropical Indian).

variability. The variance and range in the trends associated with the 20-year record are, in many cases, more than twice that of the 35-year record (compare salmon- and green-coloured distributions in Fig. 7 and Supplementary Table S3).

Moreover, globally averaged values often contrast in the direction of the trend, exhibiting upward and downward trends for the same product but over longer versus shorter time-periods. The greater variance within each product over the shorter duration (20 years) compared to the 30- and 35-year records are likely reflections of inadvertently resolving decadal and multi-decadal signals, such as the Pacific Decadal Oscillation (PDO) and El Niño Southern Oscillation (ENSO)^{38,39}.

Discussion

Scientific disagreement regarding the existence and magnitude of long-term trends in ocean wave height at a broad scale are scattered throughout the literature^{14–18,20–23}. Historical variability and discrepancies in past trends across existing global and regional-scale studies can be attributed to the type of wave data analysed (visual, satellite altimeter, numerical model hindcast, and reanalyses), time-period of analysis and analysis approach employed. The quantification of discrepancies in trend magnitudes can only be understood by systematically changing atmospheric forcing datasets applied to a single spectral wave model, systematically changing individual model settings for a given model-forcing combination and analyzing the spread across experiments.

Global atmospheric forcing. Because model settings, methods, and spatio-temporal resolutions vary unsystematically between

the opportunistic community-provided wave hindcast and reanalysis products (Table 1), we cannot attribute specific factors responsible for the ensemble inter-product variability. Based on previous research, intra-product variability might be primarily due to the different atmospheric wind forcing and data assimilation techniques used within the hindcast and/or reanalysis models respectively^{2,40}. And in fact, with this dataset, we find that historical trends obtained with products driven by CFSR wind fields were negatively biased with respect to satellite altimeter data across the time-period of analysis. The negative bias has been attributed to a temporal step-change in CFSR fields introduced by the assimilation of microwave imager wind in 1994. The negative bias of CFSR-based products compared to satellite altimeter data are especially large for H_s^{90} , which could be associated with the sampling frequency of the altimeter datasets; most satellites repeat their ground tracks once every ~3–10 days at any location on the globe¹⁵, rendering a possible under-sampling of ocean storm sea states^{18,19,41–43}. The sampling frequency has increased during the most recent decade, thus resulting in an improved representation of extremes, at the cost of a possible exaggerated trend for the period considered here.

Natural climate variability. While not explored in this analysis, past research suggests that increasing sea surface temperatures and the expansion of the tropical wind belt owing to increased radiative forcing^{44–46} during the past decades could be responsible for the historical wave climate changes presented. Although some of these changes could be attributed to multidecadal and interdecadal climate variability (e.g., Atlantic Multidecadal Oscillation—AMO and Pacific Decadal Oscillation—PDO)^{47,48}, the predictability of

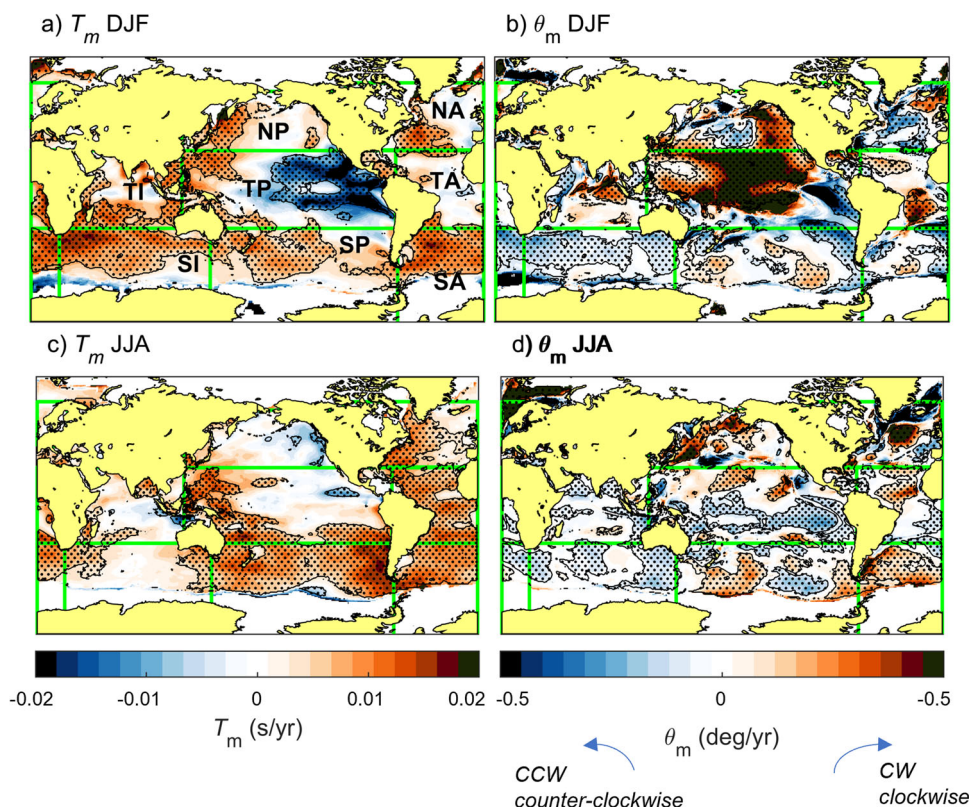


Fig. 5 Mean wave period trends (T_m) based on the 5-member ensemble and mean wave direction (θ_m) trends based on the 7-member ensemble for 1980–2014. a Median T_m for DJF season, b median θ_m for DJF season, c median T_m for JJA season, d median θ_m for JJA season. Stippling indicates regions of robust trends (multi-member ensemble mean > inter-member standard deviation; see the “Methods” section). See Fig. 4 for the definition of large-scale ocean regions.

Table 2 Ensemble mean trends (cm per year) and percent area experiencing robust signals of H_s change for the DJF season.

Region	H_s^{50} DJF				H_s^{90} DJF			
	Positive trend (cm/yr)		Negative trend (cm/yr)		Positive trend (cm/yr)		Negative trend (cm/yr)	
	% area	Mean	% area	Mean	% area	Mean	% area	Mean
NP	23	0.66 ± 0.37	15	-1.12 ± 0.43	33	1.19 ± 0.63	19	-1.32 ± 0.48
NA	23	0.68 ± 0.24	20	-0.87 ± 0.36	10	1.01 ± .35	21	-1.07 ± 0.41
TP	40	0.43 ± 0.15	4	-0.68 ± 0.33	32	0.58 ± 0.22	8	-0.97 ± 0.50
TA	49	0.39 ± 0.14	3	-0.65 ± 0.36	39	0.56 ± 0.21	5	-0.95 ± 0.52
TI	71	0.37 ± 0.12	1	-0.20 ± 0.07	69	0.58 ± 0.20	1	-0.21 ± 0.06
SP	49	0.73 ± 0.27	0	-0.33 ± 0.11	42	1.06 ± 0.44	0	-0.48 ± 0.44
SA	46	0.75 ± 0.30	0	-0.32 ± 0.15	39	1.15 ± 0.49	0	-0.62 ± 0.32
SI	47	0.67 ± 0.22	0	-0.28 ± 0.20	33	1.16 ± 0.43	0	-0.67 ± 0.29
Globe	38	0.58 ± 0.30	3	-0.84 ± 0.44	32	0.89 ± 0.50	5	-1.04 ± 0.51

NP North Pacific, NA North Atlantic, SP South Pacific, SA South Atlantic, TA Tropical Atlantic, TP Tropical Pacific, TI Tropical Indian Ocean, SI South Indian Ocean (Fig. 4).

intrinsic atmosphere–ocean cycles appear to be strongly affected by rising global temperatures^{49,50}.

The limited record lengths (~20 to 35 years) of these existing global and regional wave products (satellite altimeter wave datasets, numerical wave hindcasts, and reanalyses) are still insufficient to separate, and attribute, the individual and combined influences of low-frequency climate variability and climate warming on historical wave climate trends.

Implications and future directions. The robust change signals described are noteworthy on their own, but together with other important factors, such as astronomic tides, storm surges, and sea level rise, the overall coastal risks (such as erosion and flooding)

are likely much greater, if the offshore regional wave patterns translate into nearshore areas. Compound events, characterized by co-existence and/or co-locations in space and time of individual events that might be harmless on their own, can result in considerable disruption of coastal populations and ecosystems and ultimately amplify overall risk⁵¹. For instance, in regions of considerable tidal range, increases in the occurrence of high wave events increase the probability of coincident coastal storms with high tides, deemed to be the most problematic extreme conditions along many developed coastal regions, such as the Pacific Coast of North America^{52,53}. Within the context of sea-level rise, the upward trends of ocean H_s trends and frequency of storm-wave events will aggravate coastal extreme total water levels even in

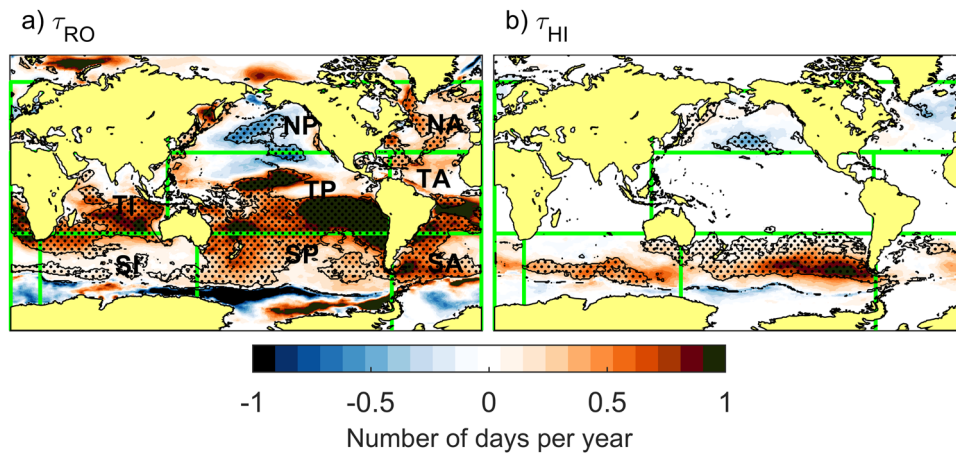


Fig. 6 Trends in the frequency of extreme wave heights based on the 7-member ensemble for 1980–2014. Annual number of **a** rough (τ_{RO}) and **b** high (τ_{HI}) wave days. Stippling indicates regions of robust trends (multi-member ensemble mean > inter-member standard deviation; (see the “Methods” section). See Fig. 4 for the definition of large-scale ocean regions.

Table 3 Ensemble mean trends (cm per year) and percent area experiencing robust signals of H_s change for the JJA season.

Region	H_s^{50} JJA				H_s^{90} JJA			
	Positive trend (cm/yr)		Negative trend (cm/yr)		Positive trend (cm/yr)		Negative trend (cm/yr)	
	% area	Mean	% area	Mean	% area	Mean	% area	Mean
NP	4	0.19 ± 0.09	30	−0.43 ± 0.16	12	0.47 ± 0.15	44	−0.72 ± 0.31
NA	41	0.32 ± 0.12	5	−0.24 ± 0.11	31	0.46 ± 0.19	12	−0.41 ± 0.17
TP	74	0.48 ± 0.22	2	−0.32 ± 0.12	67	0.68 ± 0.33	2	−0.54 ± 0.17
TA	61	0.46 ± 0.20	3	−0.31 ± 0.13	58	0.65 ± 0.30	4	−0.40 ± 0.17
TI	11	0.29 ± 0.10	6	−0.32 ± 0.14	12	0.53 ± 0.19	11	−0.36 ± 0.14
SP	45	0.80 ± 0.31	1	−0.80 ± 0.34	41	1.14 ± 0.46	0	−0.88 ± 0.46
SA	32	0.72 ± 0.29	3	−0.57 ± 0.22	29	1.04 ± 0.44	2	−0.73 ± 0.22
SI	9	0.63 ± 0.29	9	−0.53 ± 0.14	12	0.99 ± 0.35	7	−0.72 ± 0.18
Globe	37	0.53 ± 0.27	5	−0.43 ± 0.20	34	0.75 ± 0.40	7	−0.60 ± 0.29

Table 4 Ensemble mean trends and percent area experiencing robust signals of change for T_m (seconds per year) and θ_m (degrees per year) for the DJF season.

Region	T_m DJF				θ_m DJF			
	Positive trend (s/yr)		Negative trend (s/yr)		CW trend (°/yr)		CCW trend (°/yr)	
	% area	Mean	% area	Mean	% area	Mean	% area	Mean
NP	25	0.008 ± 0.003	0	−0.010 ± 0.004	45	0.28 ± 0.13	16	−0.25 ± 0.24
NA	28	0.009 ± 0.003	0	−0.004 ± 0.004	11	0.30 ± 0.19	27	−0.24 ± 0.17
TP	13	0.008 ± 0.002	30	−0.014 ± 0.005	51	0.44 ± 0.23	12	−0.33 ± 0.21
TA	19	0.008 ± 0.002	17	−0.014 ± 0.005	38	0.39 ± 0.23	13	−0.27 ± 0.20
TI	32	0.009 ± 0.003	0	NA	17	0.24 ± 0.14	15	−0.16 ± 0.09
SP	30	0.007 ± 0.002	0	−0.014 ± 0.018	14	0.13 ± 0.13	19	−0.20 ± 0.14
SA	40	0.009 ± 0.003	0	−0.011 ± 0.016	7	0.13 ± 0.14	30	−0.16 ± 0.12
SI	47	0.009 ± 0.003	0	−0.004 ± 0.001	0	0.29 ± 0.39	50	−0.13 ± 0.09
Globe	26	0.009 ± 0.003	6	−0.014 ± 0.005	20	0.34 ± 0.25	19	−0.21 ± 0.18

regions with otherwise limited water level variations⁵⁴. In addition, changes in θ_m along with coastal currents could further exacerbate coastal stability along many coastlines⁵, and in some regions, their impacts could exceed those of projected sea-level rise⁵⁵. Whereas our findings elucidate potential future conditions, we note that the 35-year record used might not exactly reflect current, and future, trends as its length could be sampling part of multi-decadal climate oscillations as previously discussed.

Whilst not directly explored here, the results shown could support past sea-level rise increases and, if trends continue, may

actually induce further sea-level rise. The increasing offshore wave activity along the West Antarctic ice shelves (Fig. 4) which are considered the most vulnerable, could potentially accelerate global sea-level rise. Increased wave-induced icequake activity, indicative of mass loss, occurs during the austral summer (DJF)⁵⁶. The results presented show a strong upward trend across the Southern Ocean wave extremes during this season (when the sea ice that attenuates swell waves is absent) than during the austral JJA winter, promoting calving. The results in this analysis suggest that West Antarctic swell-induced calving during DJF is likely

Table 5 Ensemble mean trends and percent area experiencing robust signals of change for T_m (seconds per year) and θ_m (degrees per year) for the JJA season.

Region	T_m JJA				θ_m JJA			
	Positive trend (s/yr)		Negative trend (s/yr)		CW trend ($^{\circ}$ /yr)		CCW trend ($^{\circ}$ /yr)	
	% area	Mean	% area	Mean	% area	Mean	% area	Mean
NP	5	0.009 ± 0.003	0	-0.008 ± 0.003	32	0.27 ± 0.15	8	-0.28 ± 0.19
NA	38	0.008 ± 0.002	0	-0.004 ± 0.003	22	0.42 ± 0.29	21	-0.37 ± 0.29
TP	27	0.009 ± 0.003	1	-0.007 ± 0.005	12	0.17 ± 0.09	32	-0.14 ± 0.07
TA	33	0.008 ± 0.002	1	-0.009 ± 0.004	13	0.15 ± 0.09	30	-0.12 ± 0.07
TI	15	0.006 ± 0.002	3	-0.010 ± 0.003	6	0.10 ± 0.08	31	-0.09 ± 0.06
SP	46	0.009 ± 0.003	1	-0.006 ± 0.002	21	0.14 ± 0.06	15	-0.12 ± 0.05
SA	36	0.009 ± 0.003	1	-0.006 ± 0.003	17	0.15 ± 0.10	21	-0.11 ± 0.05
SI	11	0.006 ± 0.002	0	-0.003 ± 0.001	1	0.05 ± 0.03	38	-0.09 ± 0.04
Globe	29	0.008 ± 0.003	1	-0.008 ± 0.004	15	0.23 ± 0.26	21	-0.14 ± 0.13

Table 6 Ensemble mean trends (days per year-year) and percent area experiencing robust signals of change in number of rough wave days (τ_{RO}) and high wave days (τ_{HI}).

Regions	τ_{RO}				τ_{HI}			
	Pos. trend (days/yr-yr)		Neg. trend (days/yr-yr)		Pos. trend (days/yr-yr)		Neg. trend (days/yr-yr)	
	% area	Mean	% area	Mean	% area	Mean	% area	Mean
NP	11	0.41 ± 0.22	20	-0.45 ± 0.12	9	0.12 ± 0.06	12	-0.30 ± 0.12
NA	31	0.39 ± 0.12	4	-0.32 ± 0.15	2	0.08 ± 0.04	5	-0.23 ± 0.12
TP	48	0.85 ± 0.42	2	-0.58 ± 0.12	0	0.03 ± 0.01	1	-0.07 ± 0.05
TA	45	0.75 ± 0.38	1	-0.57 ± 0.14	0	0.03 ± 0.01	0	-0.07 ± 0.05
TI	45	0.62 ± 0.21	0	-0.06 ± 0.03	0	NA	0	-0.05 ± 0.01
SP	41	0.48 ± 0.22	2	-0.68 ± 0.55	37	0.38 ± 0.29	1	-0.43 ± 0.17
SA	35	0.47 ± 0.24	1	-0.58 ± 0.48	25	0.36 ± 0.25	1	-0.31 ± 0.21
SI	29	0.35 ± 0.23	1	-0.41 ± 0.25	20	0.36 ± 0.13	1	-0.14 ± 0.06
Globe	32	0.60 ± 0.35	2	-0.46 ± 0.26	10	0.34 ± 0.25	2	-0.25 ± 0.16

increasing (possibly associated with the SAM mode^{57–59}), which would reduce buttressing and could contribute to West Antarctic ice shelf disintegration⁶⁰.

Lastly, a coordinated multi-product ensemble composed of coastal-scale numerical wave hindcasts would complement this analysis and improve our current understanding of local wave changes and their influence on coastal hazards (such as flooding and erosion). The resolution of the global wave hindcast and reanalysis products used here are insufficient to resolve nearshore wave field changes brought about by wave refraction and dissipation across complex shelf bathymetry⁶¹. Nevertheless, our findings show, with a high degree of certainty, that widespread ocean regions, including areas along coastal regions (which can serve as important proxies or indicators of nearshore conditions), are experiencing robust climatic trends. The sensitivity to duration and variance between products points to a continued need for understanding and quantifying such uncertainties as we look towards more comprehensive assessments of coastal vulnerabilities and hazards.

Conclusions

Our multiproduct ensemble of historical global wave climate samples across different atmospheric forcing and numerical wave modelling approaches, allowing a much-improved sampling of climate and model uncertainties relative to past analyses relying on one or two individual products. Relying on well-established and stringent robustness methods, we find strong signals of change during the last decades between 1980–2014 across 15–40% of the global ocean for all

combinations of wave variables and seasons. We show that regions with robust positive trends were greater than those of negative trends across most of the global ocean and that most of the Southern Hemisphere experienced robust upward trends in H_s and T_m , simultaneously, with H_s trending at a rate of up to 1–2 cm/yr. We also find strong positive trends in τ_{RO} and τ_{HI} , reaching up to ~1 day/year. The strong upward trends described are consistent with the increased ocean swell propagation from the Southern Ocean towards the tropics, due to the intensification and poleward shift of the storm belt in line with the documented positive trend of the Southern Annular Mode (SAM) over the last few decades^{58,59,62,63}.

Whereas most attention has been given to upward H_s trends, we find a general pattern of decreasing H_s across the eastern North Pacific Ocean. The decreasing trend is supported by wave buoy observations following corrections to hull and payload changes⁶⁴ and contrasts with previous analyses for which temporal step changes were unknown¹⁶ and therefore led to incorrect trends. The problem of the poorly documented instrument and/or algorithm changes, malfunctions, and/or lacking availability of such documentation is recognized by the scientific community¹³ and needs further attention before such information is lost. The long-term decrease in H_s across the eastern North Pacific Ocean and increasingly northwesterly θ_m found here is consistent with the weakening and northward shift of the jet stream since 1980 within this region⁶⁵.

On a global scale, and considering robust trends only, our results show that incident θ_m are rotating across ~40% of the global ocean, split approximately evenly between CW and CCW

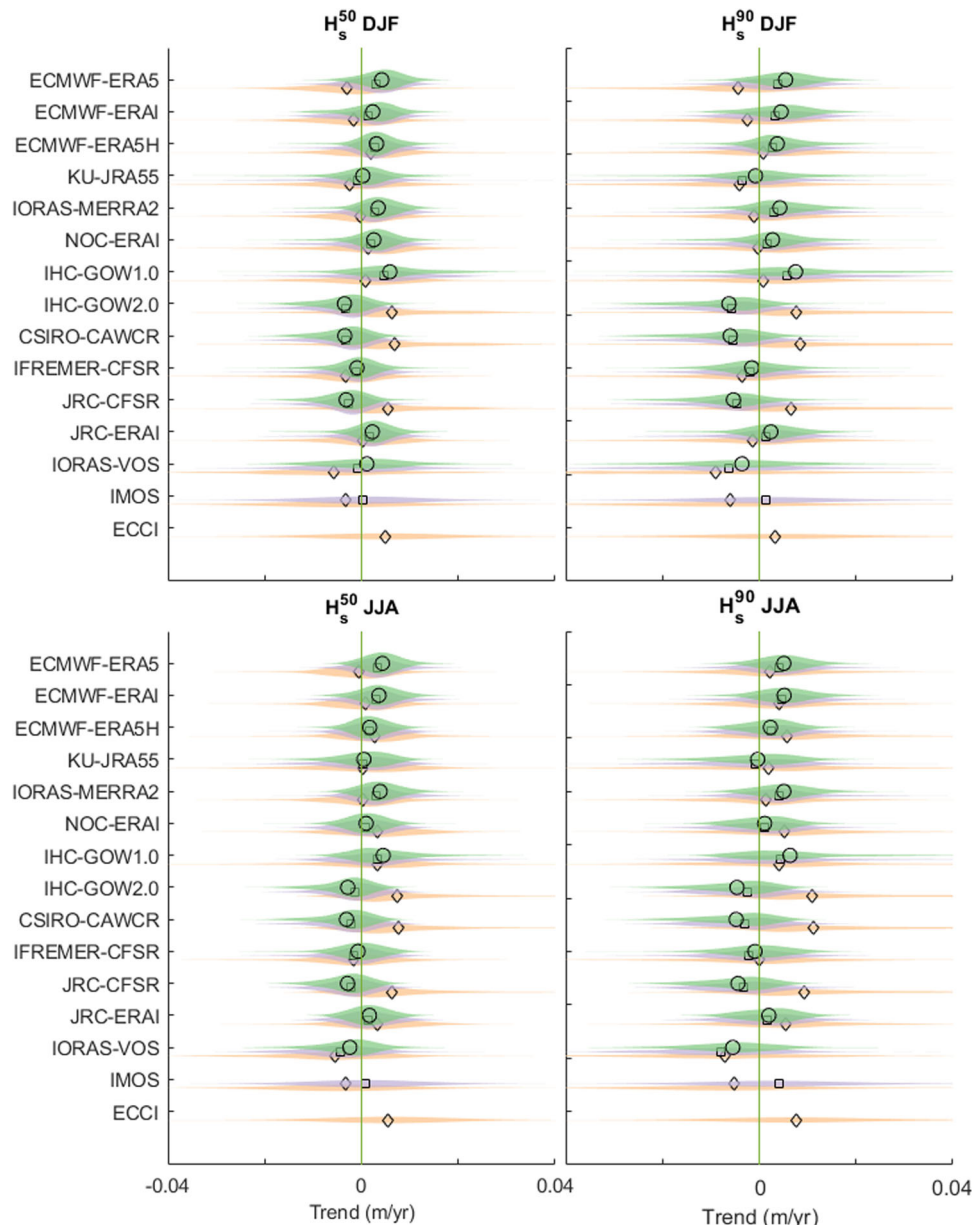


Fig. 7 Violin plots summarizing global trends of median (H_s^{50}) and 90th percentile (H_s^{90}) seasonal wave heights computed across all 15 wave state products. Globally averaged trends (symbols) and their distribution are shown for three time-periods: 1980–2014 (green fill and circles); 1985–2014 (purple and squares); 1995–2014 (orange and diamonds) for each season (JJA: June through August; DJF: December through February).

directions for DJF and JJA. There is a strong signal of CW rotations across the Central and North Pacific regions during DJF, with θ_m exceeding $\sim 0.5^\circ/\text{yr}$ within specific areas. Strong CW and CCW signals are found within the high-latitude areas of the North Hemisphere, which could be potentially associated with the well-documented changes in summer and winter sea-ice extent across the satellite records. The overall patterns of CCW rotation across the Southern Ocean during winter (DJF) are consistent with the previously described poleward shift of the extra-tropical storm belt, with swells becoming more northerly oriented.

The results presented here span a 35-year period. Trend analyses across sub-sampled periods of 20 and 30 years are found to sometimes yield drastically different results, with shorter duration results often contrasting trend signals. The larger variance across products found over a 20-year record is likely due to inadvertently capturing large-scale decadal and multi-decadal modes that contaminate trend signals, supporting

that at least 30 years of data should be used when assessing climatological wave climate trends. Finally, our analysis highlights that historical wave climate trends and climate variability inferred from single-product modelling studies^{1,66,67} can be highly misleading and need to be contextualized, otherwise the improvements in understanding the different uncertainties and providing more robust analysis of long-term climate changes will be of little benefit to current and future offshore and coastal planning.

Methods

Contributed data. Wave data were contributed to this analysis through the Coordinated Ocean Wave Climate Project (COWCLiP)^{32–34}. A key objective of COWCLiP is to provide infrastructure to support a systematic, community-based framework that allows for a systematic inter-comparison of wave products, and to make them freely accessible to the scientific community. In this study, we use wave climate statistics from the COWCLiP coordinated ensemble of contemporary global wave products³⁷. In total, we consider 12 global ocean wave products: two

reanalyses composed of numerically modelled waves and assimilated altimetry wave data, and ten numerically modelled hindcasts generated using different global atmospheric reanalysis (Table 1). Specific details on each model product are extensively described elsewhere³⁷. In addition, we use three observation datasets processed under that same framework: a ship-based observation (VOS) and two satellite altimetry (IMOS and ECC1) wave datasets. Their specific details are described in Supplementary Notes 1.

Observation-based dataset. Voluntary Observing Ship (VOS) data are particularly useful as they extend back to the late 1800s. However, the gridded VOS dataset available on a 2° resolution between 1980–2014 (see Table 1) is inherently sparse across the Southern Hemisphere due to low VOS participation and ship traffic density within the region^{68,69}. Hence, the VOS product is only used here for qualitative comparison across the Northern Hemisphere despite their inhomogeneous sampling^{68,69}. Specific details on the pre-processing of VOS data are provided in Supplementary Notes 1.

Measurement-based dataset. Satellite altimeter datasets contrast with VOS wave data by providing global coverage with regular sampling. The first altimeter product used here⁷⁰ (IMOS—Table 1) spans 32 years from 1985 to 2017 and was developed from a total of twelve cross-calibrated satellites. The second altimeter product⁷¹ (ECCI—Table 1) extends from 1992 to 2018 using a compilation of 10 satellites. These two altimeter products differ in their actual and temporal use of satellite missions, algorithms, and techniques for extracting the data, calibration methods, and network of buoys for in situ calibration. Both altimeter data products comprise aggregates of monthly H_s measurements but contain no records of T_m and θ_m . The altimeter data are thereby used as a reference, with IMOS being the main reference dataset due to its longer time-period that is commensurate with our other contributed products.

Numerical-based products. The global wave hindcast and reanalysis products are used individually and as an ensemble. These products were produced with either WaveWatchIII (WW3) or WAM spectral wave models (Table 1) based on spatio-temporally varying surface wind fields taken from different global atmospheric reanalyses (Table 1). Each forcing atmospheric reanalysis uses three or four-dimensional (3D/4D) data assimilation of in situ and remotely sensed (radiometer and scatterometers) wind speeds. The application of wind assimilations and variations throughout time in each atmospheric reanalysis is summarized in Supplementary Notes 1 and Supplementary Fig. S1.

In addition to assimilating satellite-retrieved wind data, both ERA5 and ERAI assimilate altimetry-observed H_s and are hence referred to as reanalyses. The ERA5 and ERAI datasets are part of the widely used wave products released by the European Centre for Medium-Range Weather Forecasts (ECMWF). These wave reanalysis datasets include the assimilation of altimeter H_s records from a few satellites included within the altimeter datasets. However, such wave data have been extensively re-processed^{70,71} and previous findings suggest that while some cross-over between wave-assimilated model products and pure satellite data exist, both products can have opposing trend directions and be considered as independent realizations of H_s ¹⁸.

Almost all contributing datasets have undergone previous validation and show to perform well but with variability in product-skill depending on location^{23,72–79}. Further testing of their skill is beyond the scope of our analysis, and in any event is still subject to its own specific caveats, as observations are often subject to inconsistencies in processing and data quality as previously documented. These types of inconsistencies and issues motivate the use of different products to evaluate commonality between members of an ensemble as is being done here.

Historical trend analysis. Trends were determined on seasonal statistics time-series at each grid cell. To allow for ensemble averaging, data were gridded to a common 0.5° resolution grid using a Delaunay triangulation and nearest neighbour linear interpolation. All wave height products were additionally re-gridded to a common 2° resolution grid for direct comparison to the lower resolution altimeter and VOS datasets. In cases when the original resolution product was interpolated onto a coarser grid resolution, a low-pass filter with a wavelength twice that of the new resolution was applied. Before fitting trend lines to each grid cell time-series, a 3-year moving average was applied^{80,81} to reduce natural (atmospheric) decadal and multidecadal variability (such as PDO and ENSO, which have cycles of ~10 years and ~2–7 years, respectively). The directional wave data were further treated to prevent spurious trends introduced by the circular transition of 0 to 360°, and vice versa.

Trends were computed with Sen's slope estimator⁸² in conjunction with Mann–Kendall (MK) test⁸³ for significance and confidence. Sen's slope estimates are considered more robust compared to the commonly used least-squares estimate. The MK test is used to identify the existence of a monotonic upward or downward trend over time by testing if the slope of the estimated linear regression line differs from zero. The MK test is non-parametric (i.e., distribution-free) and does not require that the residuals of the fitted regression line be normally distributed. However, the p -values calculated from the MK test assume that observations are independent realizations, free of temporal auto- or serial

correlation. In this study, the influence of auto-correlations on trends (and their significance) have been reduced using a well-established methodology^{15,84}. A prewhitened time-series (W_t) that possesses the same trend as that of the original signal is computed and recomputed (via an iterative approach) to find the best fit line and adjusted p -value:

$$W_t = \frac{(Y_t - cY_{t-1})}{(1 - c)} \quad (1)$$

where c is the lag-1 autocorrelation of the time-series, t is the time-step, Y_t is the linear fit through the time-series: $Y_t = a + bt + X_t$, with a and b representing the intercept and slope, respectively, and $X_t = cX_t + \varepsilon_t$. For each time-series at each grid cell, the analyses begin with obtaining a first estimate of $c(c_0)$ by taking the lag-1 auto-correlation of the original time-series. If $c_0 < 0.05$, the effect of serial correlation is considered negligible and iterations are then considered unnecessary. Otherwise, a trend analysis is done on the pre-whitened time-series W_t to obtain a first estimate of b_0 . The trend is subsequently removed from Y_t , and c re-computed as the lag-1 auto-correlation of the time-series $(Y_t - b_0 \cdot t)$. Iterations are continued until $|(c_t - c_{t-1})|$ and $|(b_t - b_{t-1})|$ are both $< 1\%$.

Model skill statistics. To assess model variability and skill, the satellite IMOS dataset⁷⁰ covering 30 years between 1985–2014 was used as a common reference. Skill statistics (bias and uRMSD) were computed on trends using all ocean grid cells across the common 2° grid for all products listed in Table 1, as following:

$$\text{bias} = \frac{\sum_{i=1}^N (s_{\text{mod}} - s_{\text{sat}})^i}{N} \quad (2)$$

$$\text{uRMSD} = \frac{\sum_{i=1}^N [(s_{\text{mdl}}^i - s_{\text{mdl}}) - (s_{\text{sat}}^i - s_{\text{sat}})]^2}{N} \quad (3)$$

The bias and uRMSD skill values are summarized in Fig. 8. Of note are that skill scores of the VOS data relative to the satellite altimeter data are substantially worse compared to those of the hindcast and reanalyses wave products. We attribute this difference to a lack of VOS data over the Southern Hemisphere (Supplementary Notes 3 Figs. S4, S5), which results in a greater weighting of skill to the Northern Hemisphere compared to the other ensemble members as well as less frequent and accurate estimates of wave extremes.

Skill of CFSR-driven contributed products. Examination of individual product skills and evaluation of atmospheric forcing variables shows that all CFSR-driven products in Table 1 contain a negative bias of trend (Figs. 7 and 8) compared to the IMOS altimeter reference product. In contrast, nearly all other products (except the VOS and JRA55) are clustered and positively biased across all combinations of seasons and wave height statistics. The opposing trend directions due to the use of CFSR including the time-period prior to 1994 are further supported by comparing results from the two JRC products, which differ only in the atmospheric wind forcing used (Table 1—JRC-ERAI and JRC-CFSR). A direct comparison of the trends between these products elucidates the strong dependence of winds on dynamic downscaling of ocean waves as demonstrated by the opposing trend directions for the longer 35-year time-series of H_s^{90} trends (Fig. 7). That is, the CFSR-driven JRC wave hindcast results in -0.53 ± 0.80 and -0.44 ± 0.67 cm/year for the DJF/JJA seasons respectively, whilst the ERAI-driven JRC wave hindcast exhibits positive trends $+0.24 \pm 0.67$ and $+0.20 \pm 0.56$ cm/year over the same time-period (1980–2015).

The negative bias of all CFSR-driven wave products is related to the time-period used in the trend analysis and inclusion of the south ocean basins; CFSR winds include a step-change in 1994^{85–87} brought about by introducing assimilation of microwave imager wind data⁸⁷ to reduce previously noted biases across the Southern Ocean²³. The influence on the H_s trends is particularly noticeable across the Southern Hemisphere as shown by dominantly negative trends of CFSR-driven products compared to the other products (Figs. S4 and S5). Additionally, swell generated across the Southern Ocean propagates into the North Pacific and North Atlantic regions¹² so that Southern Hemisphere wind biases translate to the global wave fields. The step change was ameliorated in the IFREMER-CFSR wave product²³ (Table 1) and is reflected in the lower bias as compared to the other CFSR-driven products.

Ensemble selection

Observation-based datasets. The altimeter and VOS datasets are used for reference purposes solely, owing to either the shorter record duration as previously discussed or the limited spatial extent relative to the wave hindcast and reanalysis products. Although the VOS wave dataset comprises stringent quality controls to reduce uncertainties (and errors) associated with professionally observed recorded H_s and dominant wave periods from thousands of ships traversing the ocean, this product was removed from the ensemble for two main reasons: (1) observers tend to report local wind-generated sea energy twice as often as swell and (2) most shipping routes are in the Northern Hemisphere with the Southern Hemisphere having much lower data density of observations.

Numerical-based products. Of the 12 global wave hindcasts and reanalysis products obtained from the COWCLiP ensemble³⁷, 7 members are used for the final

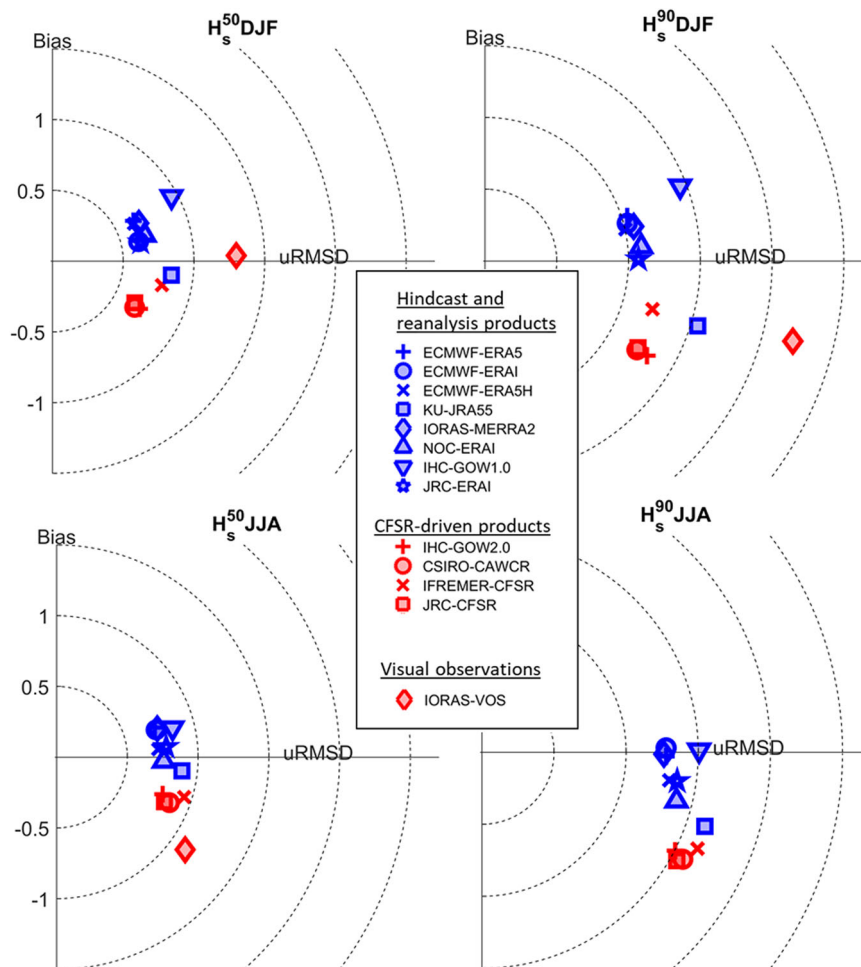


Fig. 8 Wave height trend skill statistics. Target diagrams summarizing skill statistics of 12 global wave model products and VOS compared to the reference IMOS (altimeter-derived) dataset. The horizontal axis shows the unbiased root-mean-square-error (uRMSD), and the vertical axis shows the bias (negative values indicate that hindcast/reanalysis/VOS products under-estimate compared to IMOS). The polar distance from the centre is the rmse. All units are cm per yr. Skill statistics are calculated over the time-period of the IMOS dataset, 1985 through 2014 (30 years).

ensemble. The JRC-ERA1 and JRC-CFSR products (Table 1) are removed from the ensemble because they do not include sea-ice, which could potentially introduce unrealistic trends induced by propagating wave energy from regions normally covered by sea-ice over the high southern and northern latitudes. The other CFSR-driven global products are removed owing to the step-change brought about by the wind assimilation scheme (as previously discussed). Limiting CFSR-driven global wave products to the post-1994 time-period for inclusion within the ensemble-generated trends is not considered here, because their record lengths would reduce to 20 years and contaminate the overall ensemble as previously discussed.

Furthermore, a comparison of the two altimeter products suggests that the IMOS altimeter reference data may also be negatively biased as is seen by comparing the IMOS and ECCI altimeter datasets over the shorter 21-year time-period (Fig. 7). This has also been previously documented¹⁸ over the 26-year period from 1992 to 2017, therefore suggesting that CFSR-based trends over this period, and considering the global ocean in its entirety, are likely even more negatively biased relative to true conditions than discussed here (e.g., Fig. 8). The introduction of altimeter H_s data within the ECMWF-ERA1 product (starting in August 1991) is known to also have imposed a temporal step change in trends²¹, but compared to IMOS is slightly positively biased (<0.20 m) and to a much smaller level compared to CFSR-driven global wave products (Fig. 8; particularly for H_s^{90} JJA). For this reason, the ECMWF-ERA1 was not removed from the ensemble.

In all, the ensemble is reduced to 7 members, each of which are attributed equal weight within the ensemble. By removing members recognized as likely having unrealistic trends across this specific time-period of analysis compared to the altimeter H_s data, we are able to place increased confidence in the interpreted trends of H_s and the other wave parameters derived from this coherent ensemble.

Robustness criteria. The IPCC AR5 WG1³⁶ summarizes the most commonly accepted and documented approaches for assessing and quantifying robustness associated with multi-product climate ensembles. Whereas a universally accepted

methodology is not yet agreed upon by the scientific community, we selected an often-referenced method⁸⁸, noting that other similar methods result in consistent findings³⁶. In this method, ensemble trends are deemed robust when the multi-member ensemble mean is greater than the inter-member standard deviation. To confirm that similar findings would be realized using different robustness measures, we repeated computations, following another established method³⁵, with the requirement that >50% of the models (4 out of 7) exhibit significant trends ($p_{\text{val}} < 0.05$) and at least 80% of those (>3) agree on the direction of change (Supplementary Notes 5 Tables S4–S8 and Figs. S7–S9). Given that the final ensemble considered in this analysis was reduced to a relatively small set of 7 members (see the section “Robustness criteria”), this latter method of robustness was not used as the main criteria but instead used to evaluate the influence of such criteria on the overall patterns. The overall general patterns of robustness were similar (Supplementary Notes 5 Tables S4–S8 and Figs. S7–S9) but usually covered 10–15% less ocean area, depending on the wave variable.

Code availability

The COWCLIP codes for standardized computation of statistics can be found at: <https://cowclip.org/data-access/>. Matlab codes for computing Sen’s slope and statistical significance can be found at: <https://osf.io/cwkuz/> and <http://www.mathworks.com/matlabcentral/fileexchange/authors/23983>. Matlab codes for generating violin plots are available for download at <https://www.mathworks.com/matlabcentral/fileexchange/72424-violin>. Matlab codes for circular statistics such as circular means and standard deviations of directional data are available for download at: www.kyb.mpg.de/~berens/circStat.html

Data availability

The COWCLIP archived dataset of global wave hindcasts and reanalysis products can be accessed via a Scientific Data online repository at: <https://doi.org/10.26198/3kcc-2g7137>.

Received: 16 December 2020; Accepted: 2 December 2022;

Published online: 21 December 2022

References

- Reguero, B. G., Losada, I. J. & Méndez, F. J. A recent increase in global wave power as a consequence of oceanic warming. *Nat. Commun.* **10**, 205 (2019).
- Morim, J. et al. Robustness and uncertainties in global multivariate wind-wave climate projections. *Nat. Clim. Change* **9**, 711–718 (2019).
- Storlazzi, C. D. et al. Most atolls will be uninhabitable by the mid-21st century because of sea-level rise exacerbating wave-driven flooding. *Sci. Adv.* **4**, eaap9741 (2018).
- Hoek, R. K. et al. Widespread inundation of Pacific islands triggered by distant-source wind-waves. *Global Planet. Change* **108**, 128–138 (2013).
- Sierra, J. P. & Casas-Prat, M. Analysis of potential impacts on coastal areas due to changes in wave conditions. *Clim. Change* **124**, 861–876 (2014).
- Melet, A. et al. Contribution of wave setup to projected coastal sea level changes. *J. Geophys. Res.* **125**, e2020JC016078 (2020).
- Melet, A., Meyssignac, B., Almar, R. & Le Cozannet, G. Under-estimated wave contribution to coastal sea-level rise. *Nat. Clim. Change* **8**, 234–239 (2018).
- Merkens, J.-L., Reimann, L., Hinkel, J. & Vafeidis, A. T. Gridded population projections for the coastal zone under the Shared Socioeconomic Pathways. *Global Planet. Change* **145**, 57–66 (2016).
- Bugnot, A. B. et al. Current and projected global extent of marine built structures. *Nat. Sustain.* <https://doi.org/10.1038/s41893-020-00595-1> (2020).
- Gentry, R. R. et al. Mapping the global potential for marine aquaculture. *Nat. Ecol. Evol.* **1**, 1317–1324 (2017).
- Sardain, A., Sardain, E. & Leung, B. Global forecasts of shipping traffic and biological invasions to 2050. *Nat. Sustain.* **2**, 274–282 (2019).
- Alves, J.-H. G. M. Numerical modeling of ocean swell contributions to the global wind-wave climate. *Ocean Model.* **11**, 98–122 (2006).
- Ardhuin, F. et al. Observing Sea States. *Front. Mar. Sci.* **6**, <https://doi.org/10.3389/fmars.2019.00124> (2019).
- Young, I. R. & Ribal, A. Multiplatform evaluation of global trends in wind speed and wave height. *Science* **364**, 548–552 (2019).
- Wang, X. L. & Swail, V. R. Trends of Atlantic Wave Extremes as simulated in a 40-yr wave hindcast using kinematically reanalyzed wind fields. *J. Clim.* **15**, 1020–1035 (2002).
- Ruggiero, P., Komar, P. D. & Allan, J. C. Increasing wave heights and extreme value projections: the wave climate of the U.S. Pacific Northwest. *Coast. Eng.* **57**, 539–552 (2010).
- Lin, Y. & Oey, L. Global trends of sea surface gravity wave, wind, and coastal wave setup. *J. Clim.* **33**, 769–785 (2019).
- Timmermans, B. W., Gommenginger, C. P., Dodet, G. & Bidlot, J. R. Global wave height trends and variability from new multimission satellite altimeter products, reanalyses, and wave buoys. *Geophys. Res. Lett.* **47**, e2019GL086880 (2020).
- Takbash, A. & Young, I. R. Global ocean extreme wave heights from spatial ensemble data. *J. Clim.* **32**, 6823–6836 (2019).
- Timmermans, B. W., Gommenginger, C. P., Dodet, G. & Bidlot, J. R. Global wave height trends and variability from new multimission satellite altimeter products, reanalyses, and wave buoys. *Geophys. Res. Lett.* **47**, <https://doi.org/10.1029/2019gl086880> (2020).
- Aarnes, O. J., Abdalla, S., Bidlot, J.-R. & Breivik, Ø. Marine wind and wave height trends at different ERA-interim forecast ranges. *J. Clim.* **28**, 819–837 (2015).
- Meucci, A., Young, I. R., Aarnes, O. J. & Breivik, Ø. Comparison of wind speed and wave height trends from twentieth-century models and satellite altimeters. *J. Clim.* **33**, 15 (2020).
- Stopa, J. E., Ardhuin, F., Stutzmann, E. & Lecocq, T. Sea state trends and variability: consistency between models, altimeters, buoys, and seismic data (1979–2016). *J. Geophys. Res. Oceans* **124**, 3923–3940 (2019).
- Campos, R. M., Alves, J. H. G. M., Guedes Soares, C., Guimaraes, L. G. & Parente, C. E. Extreme wind-wave modeling and analysis in the south Atlantic ocean. *Ocean Model.* **124**, 75–93 (2018).
- Ramon, J., Lledó, L., Torralba, V., Soret, A. & Doblas-Reyes, F. J. What global reanalysis best represents near-surface winds? *Q. J. R. Meteorol. Soc.* **145**, 3236–3251 (2019).
- Torralba, V., Doblas-Reyes, F. J. & Gonzalez-Reviriego, N. Uncertainty in recent near-surface wind speed trends: a global reanalysis intercomparison. *Environ. Res. Lett.* **12**, 114019 (2017).
- Stopa, J. E. & Cheung, K. F. Intercomparison of wind and wave data from the ECMWF Reanalysis Interim and the NCEP Climate Forecast System Reanalysis. *Ocean Model.* **75**, 65–83 (2014).
- Stopa, J. E., Ardhuin, F., Babanin, A. & Zieger, S. Comparison and validation of physical wave parameterizations in spectral wave models. *Ocean Model.* **103**, 2–17 (2016).
- Stopa, J. E. Wind forcing calibration and wave hindcast comparison using multiple reanalysis and merged satellite wind datasets. *Ocean Model.* **127**, 55–69 (2018).
- Shope, J. B., Storlazzi, C. D., Erikson, L. H. & Hegermiller, C. A. Changes to extreme wave climates of islands within the Western Tropical Pacific throughout the 21st century under RCP 4.5 and RCP 8.5, with implications for island vulnerability and sustainability. *Global Planet. Change* **141**, 25–38 (2016).
- Vitousek, S., Barnard, P. L., Limber, P., Erikson, L. & Cole, B. A model integrating longshore and cross-shore processes for predicting long-term shoreline response to climate change. *J. Geophys. Res. Earth Surf.* **122**, 782–806 (2017).
- Hemer, M., Erikson, L., Wang, X., Webb, A. & COWCLiP contributors. *Report of the 2018 Meeting for the WCRP-JCOMM Coordinated Ocean Wave Climate Project (COWCLiP)* (2018). JCOMM Technical Report 92. (World Meteorological Organization, 2018).
- Hemer, M., Wang, W., Charles, E., Hegermiller, C. & COWCLiP contributors. *Report of the 2014 Meeting for the WCRP-JCOMM Coordinated Global Wave Climate Projections (COWCLiP)* (2014). JCOMM Technical Report No. 82. (World Meteorological Organization, 2014).
- Hemer, M. A., Wang, X. L., Weisse, R. & Swail, V. R. Advancing wind-waves climate science: the COWCLiP Project. *Bull. Am. Meteorol. Soc.* **93**, 791–796 (2012).
- Tibaldi, C., Arblaster, J. M. & Knutti, R. Mapping model agreement on future climate projections. *Geophys. Res. Lett.* **38**, <https://doi.org/10.1029/2011GL049863> (2011).
- Collins, M. E. A. in *Climate Change 2013: The Physical Science Basis* (eds Stocker, T. F. et al.) (Cambridge University Press, 2013).
- Morim, J. et al. A global ensemble of ocean wave climate statistics from contemporary wave reanalysis and hindcasts. *Sci. Data* **9**, 358 (2022).
- Yang, S. & Oh, J.-H. Effects of modes of climate variability on wave power during boreal summer in the western North Pacific. *Sci. Rep.* **10**, 5187 (2020).
- Mann, M. E., Park, J. & Bradley, R. S. Global interdecadal and century-scale climate oscillations during the past five centuries. *Nature* **378**, 266–270 (1995).
- Feng, H., Vandemark, D., Quilfen, Y., Chapron, B. & Beckley, B. Assessment of wind-forcing impact on a global wind-wave model using the TOPEX altimeter. *Ocean Eng.* **33**, 1431–1461 (2006).
- Cooper, C. K. & Forristall, G. Z. The use of satellite altimeter data to estimate the extreme wave climate. *J. Atmos. Ocean. Technol.* **14**, 254–266 (1997).
- Salcedo-Castro, J., da Silva, N. P., de Camargo, R., Marone, E. & Sepúlveda, H. H. Estimation of extreme wave height return periods from short-term interpolation of multi-mission satellite data: application to the South Atlantic. *Ocean Sci.* **14**, 911–921 (2018).
- Jiang, H. Evaluation of altimeter undersampling in estimating global wind and wave climate using virtual observation. *Remote Sens. Environ.* **245**, 111840 (2020).
- Seidel, D. J., Fu, Q., Randel, W. J. & Reichler, T. J. Widening of the tropical belt in a changing climate. *Nat. Geosci.* **1**, 21–24 (2007).
- Lu, J., Deser, C. & Reichler, T. Cause of the widening of the tropical belt since 1958. *Geophys. Res. Lett.* **36**, <https://doi.org/10.1029/2008GL036076> (2009).
- Staten, P. W. et al. Tropical widening: from global variations to regional impacts. *Bull. Am. Meteorol. Soc.* **101**, E897–E904 (2020).
- Knudsen, M. F., Seidenkrantz, M.-S., Jacobsen, B. H. & Kuijpers, A. Tracking the Atlantic Multidecadal Oscillation through the last 8,000 years. *Nat. Commun.* **2**, 178 (2011).
- Moore, G. W. K., Halfar, J., Majeed, H., Adey, W. & Kronz, A. Amplification of the Atlantic Multidecadal Oscillation associated with the onset of the industrial-era warming. *Sci. Rep.* **7**, 40861 (2017).
- Li, S. et al. The Pacific Decadal Oscillation less predictable under greenhouse warming. *Nat. Clim. Change* **10**, 30–34 (2020).
- Dima, M., Nichita, D. R., Lohmann, G., Ionita, M. & Voiculescu, M. Early-onset of Atlantic Meridional Overturning Circulation weakening in response to atmospheric CO₂ concentration. *npj Clim. Atmos. Sci.* **4**, 27 (2021).
- Marcos, M. et al. Increased extreme coastal water levels due to the combined action of storm surges and wind waves. *Geophys. Res. Lett.* **46**, 4356–4364 (2019).
- Barnard, P. L. et al. Dynamic flood modeling essential to assess the coastal impacts of climate change. *Sci. Rep.* **9**, 4309 (2019).
- Zscheischler, J. et al. Future climate risk from compound events. *Nat. Clim. Change* **8**, 469–477 (2018).
- Vitousek, S. et al. Doubling of coastal flooding frequency within decades due to sea-level rise. *Sci. Rep.* **7**, 1399 (2017).
- Coelho, C., Silva, R., Veloso-Gomes, F. & Taveira-Pinto, F. Potential effects of climate change on northwest Portuguese coastal zones. *ICES J. Mar. Sci.* **66**, 1497–1507 (2009).
- Chen, Z. et al. Ross ice shelf icequakes associated with ocean gravity wave activity. *Geophys. Res. Lett.* **46**, 8893–8902 (2019).
- Godoi, V. A. & Torres Júnior, A. R. A global analysis of austral summer ocean wave variability during SAM–ENSO phase combinations. *Clim. Dyn.* **54**, 3991–4004 (2020).

58. Marshall, A. G., Hemer, M. A., Hendon, H. H. & McInnes, K. L. Southern annular mode impacts on global ocean surface waves. *Ocean Model.* **129**, 58–74 (2018).
59. Marshall, G. J. Trends in the Southern Annular Mode from observations and reanalyses. *J. Clim.* **16**, 4134–4143 (2003).
60. Massom, R. A. et al. Antarctic ice shelf disintegration triggered by sea ice loss and ocean swell. *Nature* **558**, 383–389 (2018).
61. Hegermiller, C. A. et al. Controls of multimodal wave conditions in a complex coastal setting. *Geophys. Res. Lett.* **44**, <https://doi.org/10.1002/2017gl075272> (2017).
62. Fogt, R. L. & Marshall, G. J. The Southern Annular Mode: variability, trends, and climate impacts across the Southern Hemisphere. *WIREs Clim. Change* **11**, e652 (2020).
63. Morim, J. et al. Global-scale changes to extreme ocean wave events due to anthropogenic warming. *Environ. Res. Lett.* **16**, 074056 (2021).
64. Gemmrich, J., Thomas, B. & Bouchard, R. Observational changes and trends in northeast Pacific wave records. *Geophys. Res. Lett.* **38**, <https://doi.org/10.1029/2011GL049518> (2011).
65. Archer, C. L. & Caldeira, K. Historical trends in the jet streams. *Geophys. Res. Lett.* **35**, <https://doi.org/10.1029/2008gl033614> (2008).
66. Zheng, C.-w. et al. Global trends in oceanic wind speed, wind-sea, swell, and mixed wave heights. *Appl. Energy* **321**, 119327 (2022).
67. Kamranzad, B., Amarouche, K. & Akpinar, A. Linking the long-term variability in global wave energy to swell climate and redefining suitable coasts for energy exploitation. *Sci. Rep.* **12**, 14692 (2022).
68. Grigorieva, V. G., Gulev, S. K. & Gavrikov, A. V. Global historical archive of wind waves based on Voluntary Observing Ship data. *Oceanology* **57**, 229–231 (2017).
69. Gulev, S. K., Grigorieva, V., Sterl, A. & Woolf, D. Assessment of the reliability of wave observations from voluntary observing ships: insights from the validation of a global wind wave climatology based on voluntary observing ship data. *J. Geophys. Res. Oceans* **108**, <https://doi.org/10.1029/2002JC001437> (2003).
70. Ribal, A. & Young, I. R. 33 years of globally calibrated wave height and wind speed data based on altimeter observations. *Sci. Data* **6**, 77 (2019).
71. Dodet, G. et al. The Sea State CCI dataset v1: towards a sea state climate data record based on satellite observations. *Earth Syst. Sci. Data* **12**, 1929–1951 (2020).
72. Brichenno, L. M. & Wolf, J. Future wave conditions of Europe, in response to high-end climate change scenarios. *J. Geophys. Res. Oceans* **123**, 8762–8791 (2018).
73. Mori, N., Shimura, T., Kamahori, H. & Chawla, A. Historical wave climate hindcasts based on JRA-55. *Proc. Coastal Dynamics '17* (eds Aagaard, T., Deigaard, R. and Furman, D.), 117–124 (Coastal Dynamics, 2017).
74. Shimura, T., Mori, N. & Hemer, M. A. Variability and future decreases in winter wave heights in the Western North Pacific. *Geophys. Res. Lett.* **43**, 2716–2722 (2016).
75. Grigorieva, V. G., Gulev, S. K. & Sharmar, V. D. Validating ocean wind wave global hindcast with visual observations from VOS. *Oceanology* **60**, 9–19 (2020).
76. Bidlot, J. R., Lemos, G., Semedo, A. ERA5 reanalysis and ERA5-based ocean wave hindcast. Paper presented at: 2nd International Workshop on Waves, Storm Surges, and Coastal Hazards. VIC, Australia, University of Melbourne, R1; Melbourne, Australia (2019).
77. Smith, G. A. et al. Global wave hindcast with Australian and Pacific Island Focus: from past to present. *Geosci. Data J.* <https://doi.org/10.1002/gdj3.104> (2020).
78. Reguero, B. G., Menéndez, M., Méndez, F. J., Mínguez, R. & Losada, I. J. A Global Ocean Wave (GOW) calibrated reanalysis from 1948 onwards. *Coast. Eng.* **65**, 38–55 (2012).
79. Perez, J., Menendez, M. & Losada, I. J. GOW2: a global wave hindcast for coastal applications. *Coast. Eng.* **124**, 1–11 (2017).
80. Hegerl, G. C. et al. Causes of climate change over the historical record. *Environ. Res. Lett.* **14**, <https://doi.org/10.1088/1748-9326/ab4557> (2019).
81. Wu, T., Hu, A., Gao, F., Zhang, J. & Meehl, G. A. New insights into natural variability and anthropogenic forcing of global/regional climate evolution. *npj Clim. Atmos. Sci.* **2**, <https://doi.org/10.1038/s41612-019-0075-7> (2019).
82. Sen, P. K. Estimates of the regression coefficient based on Kendall's Tau. *J. Am. Stat. Assoc.* **63**, 1379–1389 (1968).
83. Mann, H. B. Nonparametric tests against trend. *Econometrica* **13**, 245–259 (1945).
84. Wang, X. L. & Swail, V. R. Changes of extreme wave heights in Northern Hemisphere Oceans and related Atmospheric Circulation Regimes. *J. Clim.* **14**, 2204–2221 (2001).
85. Rasche, N. & Ardhuin, F. A global wave parameter database for geophysical applications. Part 2: Model validation with improved source term parameterization. *Ocean Model.* **70**, 174–188 (2013).
86. Chawla, A., Spindler, D. M. & Tolman, H. L. Validation of a thirty year wave hindcast using the climate forecast system reanalysis winds. *Ocean Model.* **70**, 189–206 (2013).
87. Saha, S. et al. The NCEP climate forecast system reanalysis. *Bull. Am. Meteorol. Soc.* **91**, 1015–1058 (2010).
88. Hemer, M. A., Fan, Y., Mori, N., Semedo, A. & Wang, X. L. Projected changes in wave climate from a multi-model ensemble. *Nat. Clim. Change* **3**, 471–476 (2013).

Acknowledgements

This analysis comprises Task 1 of the Coordinated Ocean Wave Climate Project (COWCLIP: <https://cowclip.org/>). COWCLIP is an international collaborative working group—endorsed by the Joint Technical Commission for Oceanography and Marine Meteorology, a partnership between the World Meteorological Organization and the Intergovernmental Oceanographic Commission of UNESCO. We especially acknowledge the groups that contributed data products to this study: European Centre for Medium-Range Weather Forecasts (ECMWF), Kyoto University (KU), Institute of Oceanology of Russian Academy of Sciences (IORAS), National Oceanography Centre of the UK (NOC), Institute of Hydraulics Cantabria (IHC), Australian Commonwealth Scientific and Industrial Research Organisation (CSIRO), French National Institute for Ocean Sciences (IFREMER), European Commission's Joint Research Centre (JRC), Australian Integrated Marine Observing System (IMOS), and the European Space Agency (ESCI). We also thank COWCLIP participants, including Paula Camus, for contributing ideas and edits to the text. J.M., C.T., and M.H. acknowledge the support of the Australian Government National Environmental Science Programme Earth Systems and Climate Change Hub. J.M. acknowledges the support of the University of Central Florida Pre-eminent Programme (P3) and the NASA Seal Level Science Programme. J.M. and L.E. acknowledge the support of the US Geological Survey Coastal and Marine Hazards/ Resources Programme.

Author contributions

L.E. and J.M. wrote the core of the manuscript and co-led the data synthesis and its analysis. M.H. and I.Y. contributed to the writing of the manuscript and data analysis. X.W. and L.M. developed the codes for consistent processing. C.T., O.A., Ø.B., J.-R.B., V.G., V.S., L.M., M.Menendez, M.Markina, J.S., and T.S. produced and/or post-processed the individual data products. M.H., I.Y., N.M., J.S., S.G., L.B., J.-R.B., A.S., and J.W. led modelling and/or analysis of specific individual products. C.A., N.G., S.C., and A.W. contributed to the design analysis. Any use of trade, firm, or product names is for descriptive purposes only and does not imply endorsement by the US Government.

Competing interests

The authors declare no competing interests.

Additional information

Supplementary information The online version contains supplementary material available at <https://doi.org/10.1038/s43247-022-00654-9>.

Correspondence and requests for materials should be addressed to L. Erikson.

Peer review information *Communications Earth & Environment* thanks Clea Denamiel and the other, anonymous, reviewer(s) for their contribution to the peer review of this work. Primary Handling Editor: Heike Langenberg.

Reprints and permission information is available at <http://www.nature.com/reprints>

Publisher's note Springer Nature remains neutral with regard to jurisdictional claims in published maps and institutional affiliations.



Open Access This article is licensed under a Creative Commons Attribution 4.0 International License, which permits use, sharing, adaptation, distribution and reproduction in any medium or format, as long as you give appropriate credit to the original author(s) and the source, provide a link to the Creative Commons license, and indicate if changes were made. The images or other third party material in this article are included in the article's Creative Commons license, unless indicated otherwise in a credit line to the material. If material is not included in the article's Creative Commons license and your intended use is not permitted by statutory regulation or exceeds the permitted use, you will need to obtain permission directly from the copyright holder. To view a copy of this license, visit <http://creativecommons.org/licenses/by/4.0/>.

This is a U.S. Government work and not under copyright protection in the US; foreign copyright protection may apply 2022